Gómez-Treviño *et al. Earth, Planets and Space (2018) 70:133*
https://doi.org/10.1186/s40623-018-0900-y

Earth, Planets and Space

FULL PAPER

Open Access

Invariant TE and TM magnetotelluric impedances: application to the BC87 dataset

Enrique Gómez-Treviño*, Yunuhen Muñiz, Mayra Cuellar and Armando Calderón-Moctezuma

Abstract

Invariants under rotation of the magnetotelluric impedance tensor relax the directional requirements when fitting data using two-dimensional (2D) models. This happens, for instance, when using the familiar impedance derived from the determinant of the tensor. In this work, we use two particular invariants that reduce in 2D to the traditional transverse electric (TE) and transverse magnetic (TM) impedances. They are obtained as the missing first link of an infinite chain of invariants that are computed iteratively without any reference to a strike direction. We challenge the current view that the TE and TM impedances are not invariant. We argue in favor of the invariance. We apply our approach to the well-known and difficult BC87 dataset. These data present (1) electro-galvanic distortions, (2) static shifts and (3) inconsistent strikes. To remove the electro-galvanic distortions, we use recent developments that combine the phase tensor with the quadratic equation. To handle statics, we use a mimic of the electromagnetic array profiling (EMAP) method; the property of the TE mode of acting as a natural filter for static effects, as reported recently in the literature. Finally, the multiple strikes are handled by the invariant character of the TE and TM impedances. The processed TE responses are interpreted as one-dimensional models to construct a 2D resistivity image of the subsurface, which is accompanied by the complementary image of the multiple strikes. Our model correlates very well with an independent EMAP survey over the Nelson Batholith and with seismic reflection and refraction lines.

Keywords: Invariant TE and TM, MT strike, BC87 dataset

Introduction

The magnetotelluric (MT) method of geophysical exploration as originally proposed assumed scalar data in the form of impedances defined as ratios of orthogonal electric and magnetic fields (Tikhonov 1950; Rikitake 1950; Cagniard 1953). The assumptions of a plane wave and of an electrical resistivity that varies only with depth imply that the fields can be measured in any direction as long as they are orthogonal. The impedance is said to be invariant under rotation of coordinates. On the other hand, when the resistivity distribution varies laterally this azimuthally symmetric model breaks down. The data are no longer a scalar but a 2×2 tensor whose elements depend on the coordinate system. However, it is still possible to compute scalars that are invariant under rotation and that may benefit the interpretation process. The effective impedance of Berdichevsky and Dmitriev (1976) obtained from the determinant of the tensor is the archetypical that exemplifies the incentives of using invariants in the interpretation of two-dimensional (2D) data. These assets have been illustrated by Pedersen and Engels (2005), who remarks as the most important asset that the sounding curves are the same regardless of the assumed azimuth. In fact, the sounding curves are the same regardless of the variations of azimuths from site to site and from frequency to frequency.

This work was motivated by the possibility of extending the assets of invariants to the 2D classical transverse electric (TE) and transverse magnetic (TM) induction modes. The former is associated with the current flow along strike and the latter to the flow across strike. The traditional view of the TE and TM impedances is that they depend on the strike direction, since one needs to evaluate the impedances at a given predetermined angle, either using traditional formulae as that of Swift (1967) or by fitting a distortion model to the data as in the approach of Groom and Bailey (1989). In both cases,

*Correspondence: egomez@cicese.mx
División de Ciencias de la Tierra, CICESE, Ensenada, Baja California, Mexico

the calculated impedances seem to depend on the chosen strike direction. Because of this dependence on direction the current view is that the TE and TM impedances are not invariant under rotation. However, recent developments seem to indicate that this dependence is only apparent and that it originates in the way strike and impedances are traditionally computed, either finding the strike first and then rotating accordingly, or doing it simultaneously as when using a distortion model. The fact is that strike and impedances can be decoupled from each other. Muñíz et al. (2017) combine the phase tensor of Caldwell et al. (2004) and the quadratic equation of Gómez-Treviño et al. (2014a) to obtain, independently from each other, the strike direction and the TE and TM impedances. The question is (a) how should this decoupling of the two quantities be understood and (b) how to use it in practice to improve 2D inversions of data.

The well-known BC87 dataset has several features that make it adequate for the present problem because it presents inconsistent strikes from site to site and from frequency to frequency. The dataset was acquired across the Nelson Batholith in British Colombia in 1987 using the-then state-of-the-art commercial MT equipment, was presented by Jones et al. (1988) and further processed and interpreted by Jones et al. (1993), among others. The product of a workshop, the pertinent papers were published in a special issue of Journal of Geomagnetism and Geoelectricity with an introductory paper by Jones (1993). The dataset is available at the MTNet site. It is recommended for testing ideas and advances in tools for processing and inverting MT soundings. The data are distorted by (1) electro-galvanic effects, (2) static shifts and (3) inconsistent strike directions from site to site and from frequency to frequency. In this work we deal with the distortions and the static shifts using recent developments describe in Gómez-Treviño et al. (2014a, b) and Muñíz et al. (2017). For the third problem, that of inconsistent strikes, we first provide a general proof unrelated to any angular reference to show that the TE and TM impedances must be considered invariants. We then proceed to interpret the data.

Theory

The basic unit of any MT survey is a second-order complex impedance tensor $\boldsymbol{Z}$, such that $\boldsymbol{E} = \boldsymbol{ZH}$, where $\boldsymbol{E}$ and $\boldsymbol{H}$ stand for the horizontal electric and magnetic fields, respectively. Explicitly

$$\boldsymbol{E} = \begin{pmatrix} E_x \\ E_y \end{pmatrix} = \begin{pmatrix} Z_{xx} & Z_{xy} \\ Z_{yx} & Z_{yy} \end{pmatrix} \begin{pmatrix} H_x \\ H_y \end{pmatrix} = \boldsymbol{ZH}. \tag{1}$$

Following Romo et al. (2005) we define two complex resistivities as

$$\varrho_{\mathrm{s}} = \frac{1}{2}\frac{1}{\omega\mu_0} Z_{\mathrm{s}}^2 \tag{2}$$

and

$$\varrho_{\mathrm{p}} = \frac{1}{2}\frac{1}{\omega\mu_0} Y_{\mathrm{s}}^{-2}. \tag{3}$$

Here ω stands angular frequency, μ_0 for the magnetic permeability of free space, Z_{s}^2 is the trace of $\boldsymbol{Z}^{\mathrm{T}}\boldsymbol{Z}$ and Y_{s}^{-2} is the reciprocal of the trace of $\boldsymbol{Y}^{\mathrm{T}}\boldsymbol{Y}$, where $\boldsymbol{Y} = \boldsymbol{Z}^{-1}$ is the admittance tensor. We call ϱ_{s} and ϱ_{p} the series and parallel resistivities, respectively. These resistivities are complex but their magnitudes are the same as those of the classical formulas. However, the phases of the complex resistivities are double those of the corresponding impedances because of the squared complex impedance. Both ϱ_s and ϱ_{p} are invariant under rotation of coordinates because this is a property of the trace of $\boldsymbol{Z}^{\mathrm{T}}\boldsymbol{Z}$ and $\boldsymbol{Y}^{\mathrm{T}}\boldsymbol{Y}$.

Following Gómez-Treviño et al. (2013) we define a sequence of invariants as

$$\varrho_{\mathrm{s}(i+1)} = \frac{1}{2}\left(\varrho_{\mathrm{s}i} + \varrho_{\mathrm{p}i}\right) \tag{4}$$

and

$$\frac{1}{\varrho_{\mathrm{p}(i+1)}} = \frac{1}{2}\left(\frac{1}{\varrho_{\mathrm{s}i}} + \frac{1}{\varrho_{\mathrm{p}i}}\right). \tag{5}$$

The sequence starts with $i = 1$ so that $\varrho_{\mathrm{s}1} = \varrho_{\mathrm{s}}$ and $\varrho_{\mathrm{p}1} = \varrho_{\mathrm{s}}$ are the original resistivities. As iterations proceed the new resistivities are averages of the ones computed at the previous cycle. The elementary units from which all averages come from are of course ϱ_{s} and ϱ_{p}. We now ask whether there are invariants more elementary than ϱ_{s} and ϱ_{p}. In other words: what is iteration zero? Mathematically, this can be stated as finding γ and λ such that

$$\varrho_{\mathrm{s}} = \frac{1}{2}(\gamma + \lambda) \tag{6}$$

and

$$\frac{1}{\varrho_{\mathrm{p}}} = \frac{1}{2}\left(\frac{1}{\gamma} + \frac{1}{\lambda}\right). \tag{7}$$

At this point it is important to realize that γ and λ are not part of the chain of invariants defined by Eqs. 4 and 5. We are taking a step backward. It is a working hypothesis that γ and λ do actually exist and that they might be meaningful, but there is no warrantee.

Solving for γ there results

$$\lambda^2 - 2\varrho_s\lambda + \varrho_s\varrho_p = 0. \tag{8}$$

We call the solutions $\varrho_\pm$ and are given as

$$\varrho_\pm = \varrho_s \pm \sqrt{\varrho_s^2 - \varrho_s\varrho_p}. \tag{9}$$

In Eqs. 6 and 7, the variables γ and λ can't be distinguished from each other so the solutions for γ are the same as those for λ. Equation 9 attracts and resolves the duality with the $\pm$ signs. On the other hand, multiplying ϱ_+ by ϱ_- it follows that $\varrho_+\varrho_- = \varrho_s\varrho_p$. Also, combining Eqs. 4 and 5 it follows that $\varrho_{si}\varrho_{pi} = \varrho_{s(i+1)}\varrho_{p(i+1)}$. The product $\varrho_+\varrho_-$ is then equal to the product $\varrho_{si}\varrho_{pi}$ for any iteration. In fact, the sequence converges to $\sqrt{\varrho_s\varrho_p}$, the geometric mean of ϱ_s and ϱ_p, which in turn is equal to ϱ_d, the determinant resistivity (Gómez-Treviño et al. 2013). Figure 1 illustrates the sequence and its convergence after a few iterations for site 31 of Varentsov (1998) synthetic

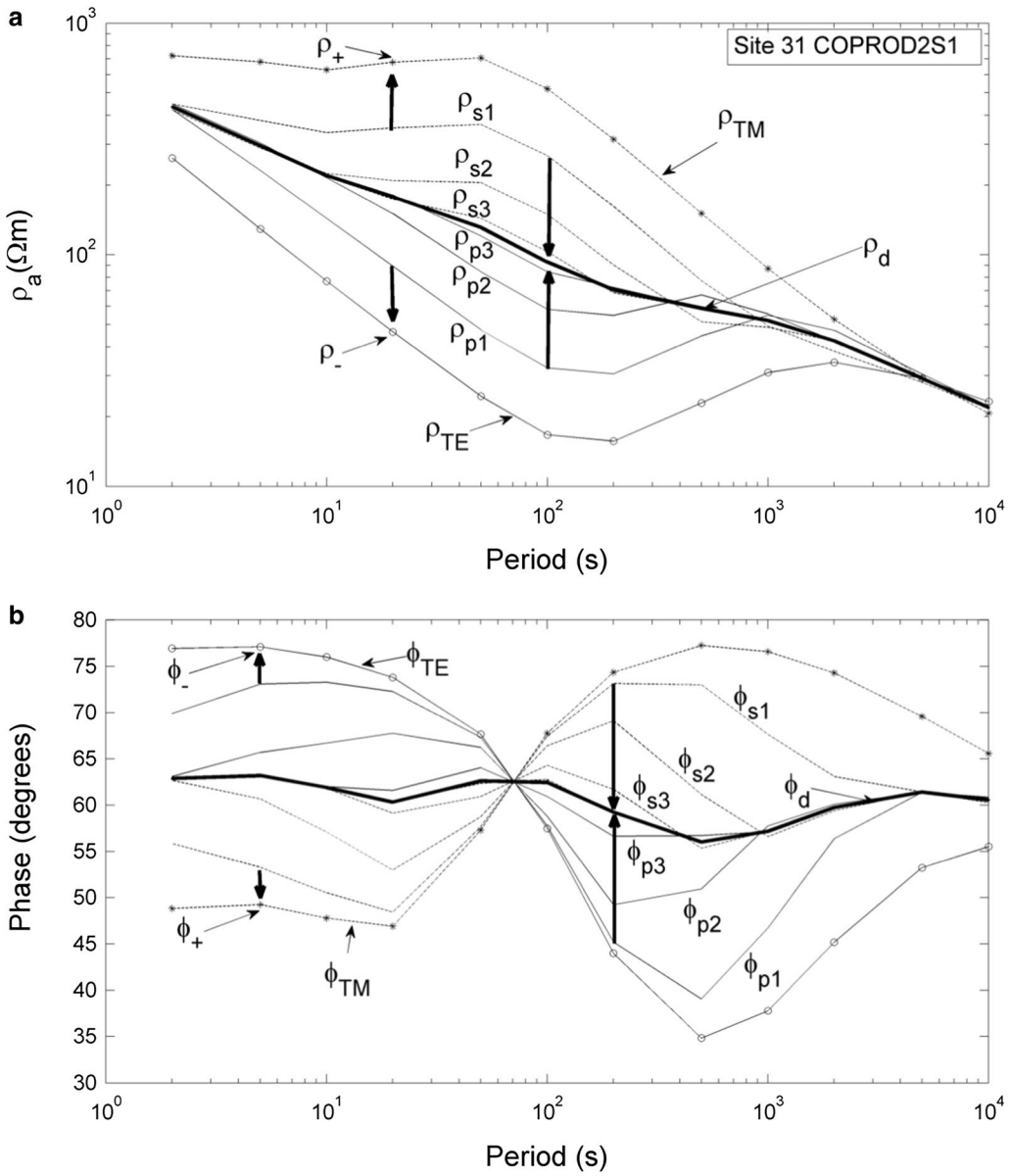

Fig. 1 Graphical illustration of the infinite chain of invariants and of the missing first link: **a** apparent resistivity curves; **b** phase curves. The longer arrows indicate the direction toward convergence of the infinite chain. The shorter arrows indicate the direction toward the missing first links given by the solution of the quadratic equation. The TE and TM resistivities coincide with ρ_- and ρ_+, respectively, but it could be the other way around

COPROD2S1 dataset. To denote the amplitude of the complex resistivities we use $\rho = |\varrho|$ with the corresponding subscripts. For the phases of $\varrho_{\pm}$ we use $\phi_{\pm}$.

The analysis above demonstrates that $\varrho_{\pm}$ are invariant under rotation and that they are the first members of an infinite family of pairs of invariants whose geometric average is the resistivity derived from the determinant. So far there has been no restriction as to the dimensionality of the data. The derivation of the quadratic Eq. 8 is completely general in the sense that it applies to any dimension. An earlier derivation of the equation in Gómez-Treviño et al. (2014a) relied on 2D analyses and extrapolation of its solution to three dimensions. In the present work we proceed from the general to the particular. In 2D the invariants ϱ_s and ϱ_p can be written as $\varrho_s = (\varrho_{TE} + \varrho_{TM})/2$ and $\varrho_p^{-1} = \left(\varrho_{TE}^{-1} + \varrho_{TM}^{-1}\right)/2)$. Substituting these expressions into Eq. 9 we obtain $\rho_+ = \rho_{TE}$ and $\rho_- = \rho_{TM}$ or $\rho_+ = \rho_{TM}$ and $\rho_- = \rho_{TE}$. It is unfortunate that this result is not unique, in the sense that the modes cannot be differentiated. However, this is how things should be. This ambiguity is consistent with the original assumption in Eqs. 6 and 7 about γ and λ, which can also exchange places, and also with the traditional ambiguity of 90°. Beyond this uncertainty, the invariants ϱ_+ and ϱ_- are the same as ϱ_{TE} and ϱ_{TM}. The outer curves in Fig. 1 illustrate this correspondence.

The elements of the impedance tensor are not invariant under rotation. This is illustrated in Fig. 2 using polar diagrams for the element Z_{xy} expressed as resistivity ρ_{xy} for the period of 1000 s of the sounding curve used in Fig. 1. We also plot the series and parallel resistivities as well as ρ_+ and ρ_-, all of which describe circles as the coordinates are rotated from 0 to 360°. The resistivity ρ_{xy} plots into the characteristic peanut shape for 2D data. We present polar diagrams for the two strikes of 0 (90) and 30 (60) degrees. Regardless of the strike, ρ_+ and ρ_- always intersect ρ_{xy} when this attains the main resistivities ρ_{TE} and ρ_{TM}. Thus, ρ_+ and ρ_- predict the resistivities of the two orthogonal modes regardless of strike.

Applications: BC87 dataset

Fit to data and predicted TE impedances

Figure 3 shows the location of the MT sites that comprise the BC87 dataset. We selected 16 soundings to make a profile 110 km long between sites 902 and 022. Also shown is the location of an EMAP line over the Nelson Batholith and three nearby sites. They will be compared below after the final analysis of the dataset. There are three issues posed by this dataset: (1) electro-galvanic distortions; (2) static shifts and (3) variable strikes. We don't deal explicitly with the first here. It was reported in Muñíz et al. (2017) using a combination of the phase tensor and the quadratic equation. We take it from there and proceed to the issue of static shifts. For this we follow Gómez-Treviño et al. (2014b) by inverting the apparent resistivity of the TM mode and the phases of both modes, and considering the TE apparent resistivity as output in

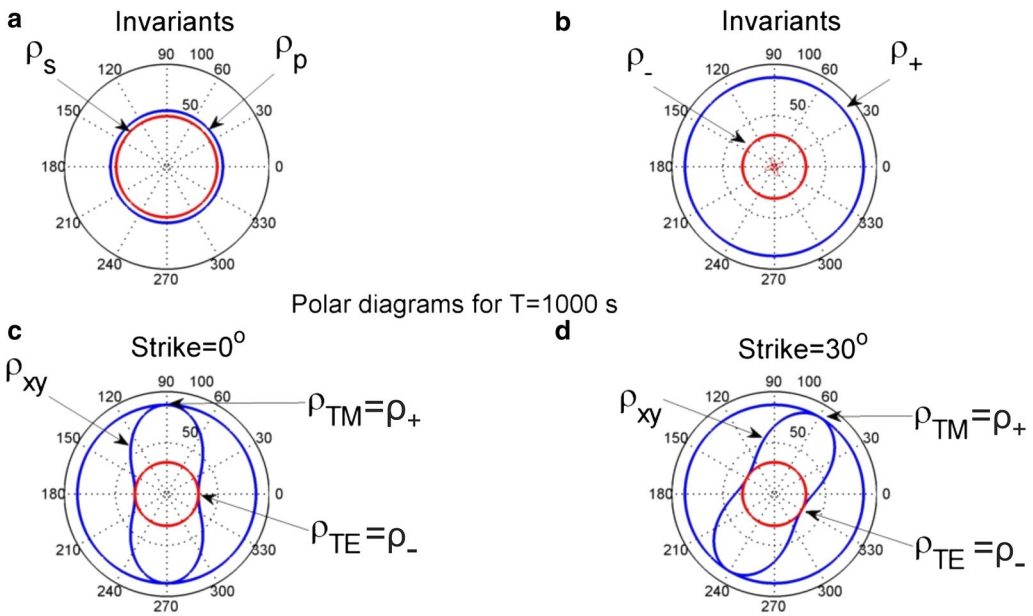

Fig. 2 Polar diagrams for: **a** the invariants ρ_s and ρ_p; **b** the invariants ρ_+ and ρ_-; **c** the element ρ_{xy} for a strike of 0° and the invariants ρ_+ and ρ_-; **d** the element ρ_{xy} for a strike of 30° and the invariants ρ_+ and ρ_-

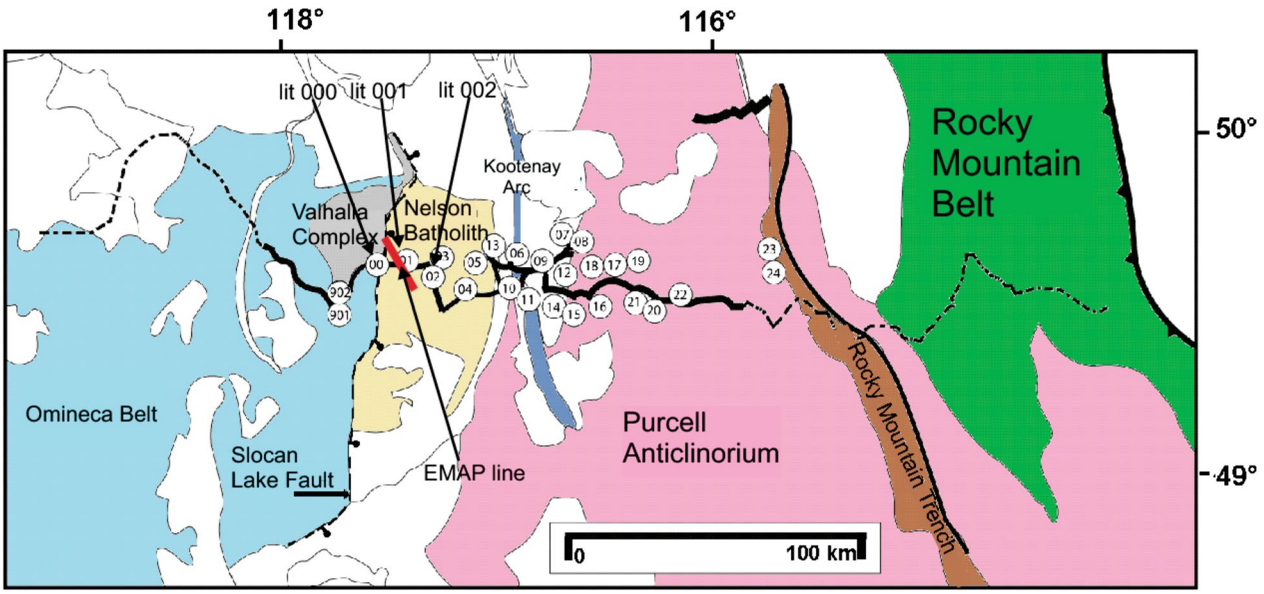

Fig. 3 Location of the MT sites of the BC87 dataset. We chose a profile 110 km long composed of 16 soundings between sites 902 and 022. The EMAP line is 10 km long and it is compared below with our results for the three indicated sites. The 16 sites are lit902, 00, 01, 02, 04, 05, 13, 06, 11, 09, 15, 16, 17, 19, 21 and 22

the inversion process. We focus here on the third issue of variable strikes. For comparison, we also consider fixed strikes, and to be unbiased about the classical ambiguity of 90° in the strike determination we analyze all possibilities.

Figures 4 and 5 present the results for the case of fixed strikes. The choices of strikes determined by Jones et al. (1993) are −30° (N30°W) or 60° (N60°E). They chose N30°W for their interpretation because that is the regional geological strike of the Canadian Cordillera. On the other hand Eisel and Bahr (1993) determine a strike of 45° (N45°E). In our case we decided to keep the ambiguity of East or West and consider both options until the end of the analysis. The option of the East is backed by the existence of deep transverse basement structural control of mineral systems at a more local level in the

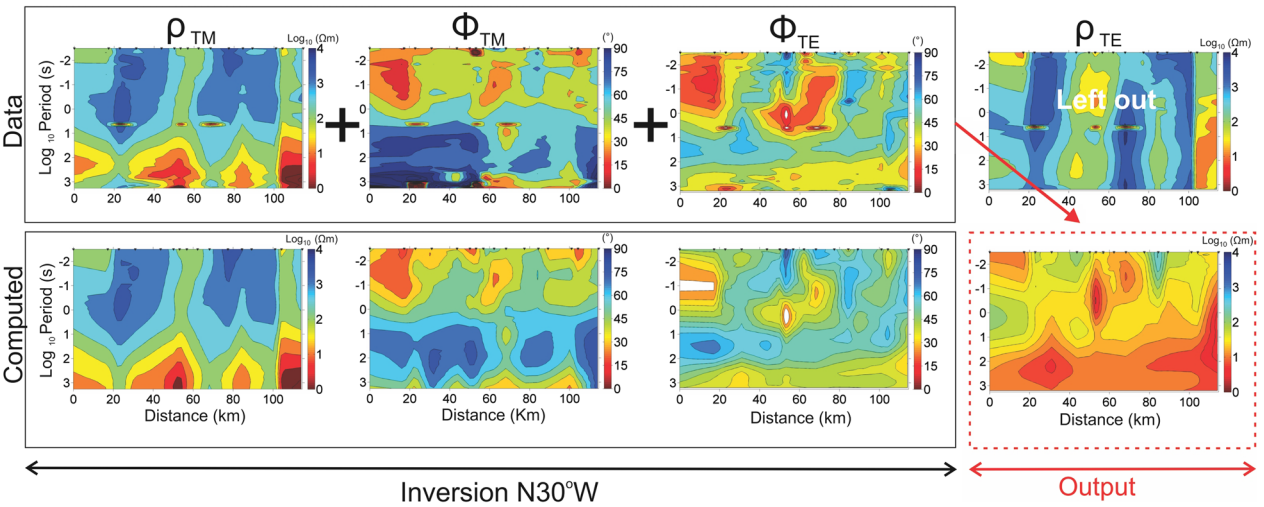

Fig. 4 Fit to the data for a strike direction of −30° or N30°W. The upper images are the data pseudo-sections and the ones below are the corresponding responses of the model. Notice that the pseudo-sections of the TE apparent resistivity don't look alike at all in this case. The other three pairs indicate a good fit to the data. The TE apparent resistivity was not part of the inversion process

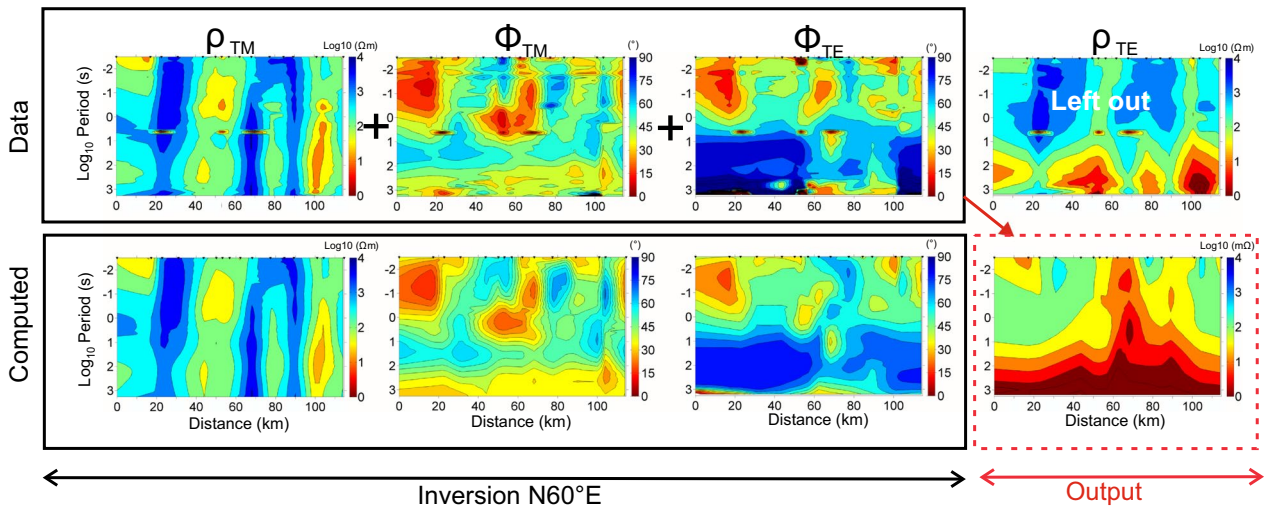

Fig. 5 Fit to the data for a strike direction of 60° or N60°E. The upper images are the data pseudo-sections and the ones below are the corresponding responses of the model. Notice that the pseudo-sections of the TE apparent resistivity look more alike than the corresponding ones of this figure. The other three pairs indicate a good fit to the data. The TE apparent resistivity was not part of the inversion process

area as reported by McMechan (2012). The impedances were computed using the STRIKE algorithm based on the work of McNeice and Jones (2001). This algorithm also removes any electro-galvanic distortions that may be present in the data so that they are ready for the second step, that of correcting for the static shifts. Figure 4 summarizes the case of strike N30°W. The upper part shows the data and the lower part the responses of the resistivity model obtained by inverting the data. For now let us center our attention around the fit to the data and on the inversion process. The input to the inverse routine is the amplitude of the TM apparent resistivity and the phases of both modes. Any static shifts of the amplitude of the TM apparent resistivity can be accommodated by electric charges placed on the walls of small cells around the electric dipoles. This is not the case for the TE mode, so we leave the apparent resistivity out of the inversion process. Details of this approach are given in Gómez-Treviño et al. (2014b). The result is a very good fit to the inverted data but not so good for those left out. In fact, the pseudo-sections for the TE apparent resistivity don't look alike at all for the strike of N30°W in Fig. 4, although they resemble each other better for the strike of N60°E in Fig. 5. Another difference worth noting is that the characteristic anomalous phases larger than 90° of this dataset fall in the TM mode for the strike N30°W and in the TE mode for the case of N60°E. The former contradicts the results of Weidelt and Kaikkonen (1994) who showed that TM phase responses of 2D models lie in the range 0–90°, and the latter coincides with Parker (2010) who proves that 2D models exist whose TE mode phase responses are outside 0–90°. This reinforces the likelihood of a strike N60°E as suggested by the dominance of local transverse structures of McMechan (2012).

We now turn to the invariants $\rho_{\pm}$. The result of identifying ρ_{-} as TM ($\rho_{-} \leftrightarrow$ TM) is shown in Fig. 6 and that of ρ_{+} with TM ($\rho_{+} \leftrightarrow$ TM) in Fig. 7. We proceeded likewise as for the case of fixed angles. Again, the result is a very good fit to the data involved in the inversion and not so good for those left out. The pseudo-sections for the TE apparent resistivity don't look alike at all for $\rho_{-} \leftrightarrow$ TM in Fig. 6, but they resemble each other very much for $\rho_{+} \leftrightarrow$ TM as shown in Fig. 7. On the other hand, by inspection one can relate N30°W with $\rho_{-} \leftrightarrow$ TM and N60°E with $\rho_{+} \leftrightarrow$ TM. This means that ρ_{-} refers to free strikes around N30°W and ρ_{+} to free strikes around N60°E. In relation to whether the strike should be toward the NW or NE we can only add at this point that the best prediction of the TE apparent resistivity data is that of $\rho_{+} \leftrightarrow$ TM which we have associated with N60°E. This is a second clue in favor of the transverse strike to the Canadian Cordillera. Before proceeding with this analysis we must explain the origin of all the computed pseudo-sections. That is, the models behind them and how they were obtained.

Roughest models

The computed pseudo-sections in the four previous figures were obtained from the corresponding four models shown in Fig. 8. The input data were the measured apparent resistivity of the TM mode and the phases of both modes. Rather than considering these models as

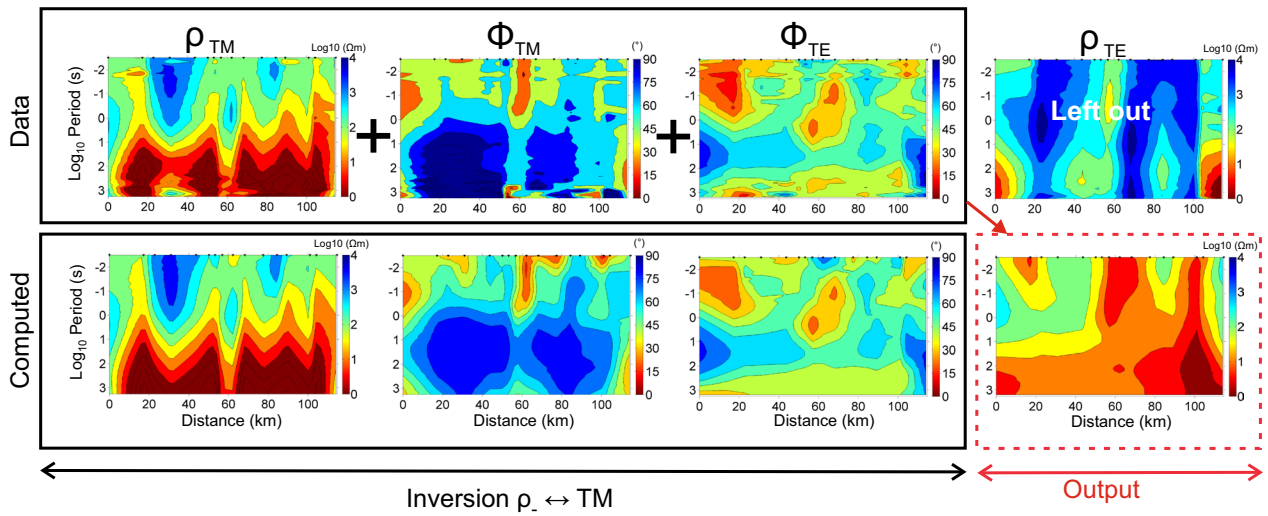

Fig. 6 Fit to the data for the invariant ρ_- assumed as the TM mode. The upper images are the data pseudo-sections and the ones below are the corresponding responses of the model. Notice that the pseudo-sections of the TE apparent resistivity don't look alike at all in this case, just as they don't for the strike of − 30° in Fig. 5. The other three pairs indicate a good fit to the data. The TE apparent resistivity was not part of the inversion process

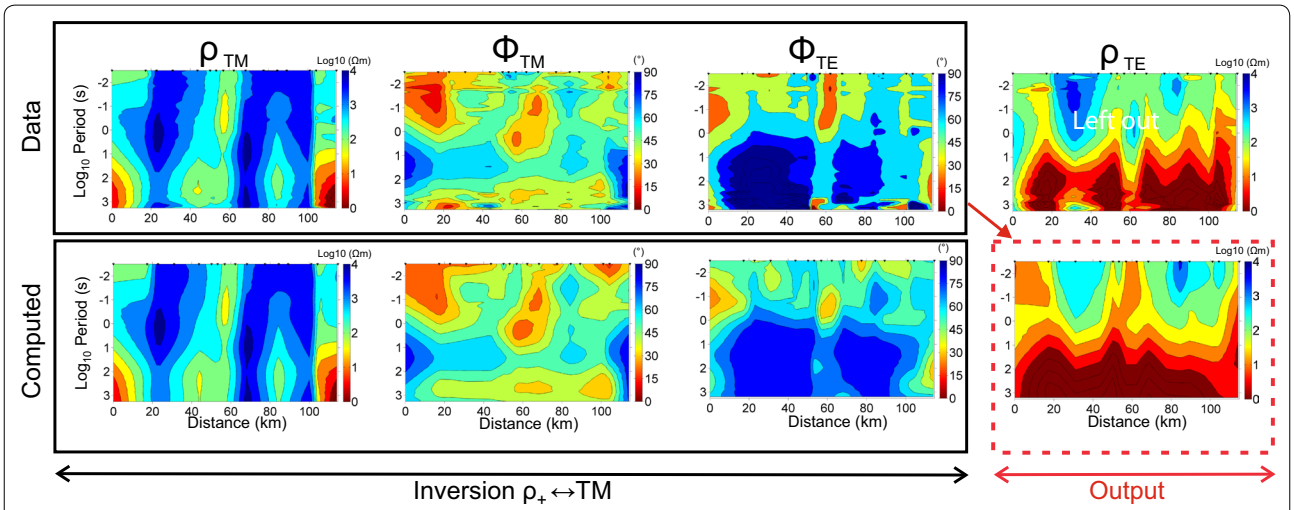

Fig. 7 Fit to the data for the invariant ρ_+ assumed as the TM mode. The upper images are the data pseudo-sections and the ones below are the corresponding responses of the model. Notice that the pseudo-sections of the TE apparent resistivity look more alike than in the previous three cases. The other three pairs indicate a good fit to the data. The TE apparent resistivity was not part of the inversion process

the output in the inversion process we use them as stepping stones to obtain the TE apparent resistivity which is free from static effects (Gómez-Treviño et al. 2014b). We monitor the geometric average of each sounding and choose the model for which there is convergence for all sites. This is illustrated in Fig. 9 where the variable tau is the regularization parameter in the inverse routine of Rodi and Mackie (2001). Traditionally, a compromise is sought between roughness of the model and fitness to the data, in such a way that the final model is smooth following Occam's philosophy (Constable et al. 1987). Instead, we seek the roughest model with the maximum possible of the larger wave numbers. The idea is to mimic Bostick's (1984, 1986) EMAP method. The roughest models are difficult to interpret visually because they would correspond to the unprocessed EMAP data.

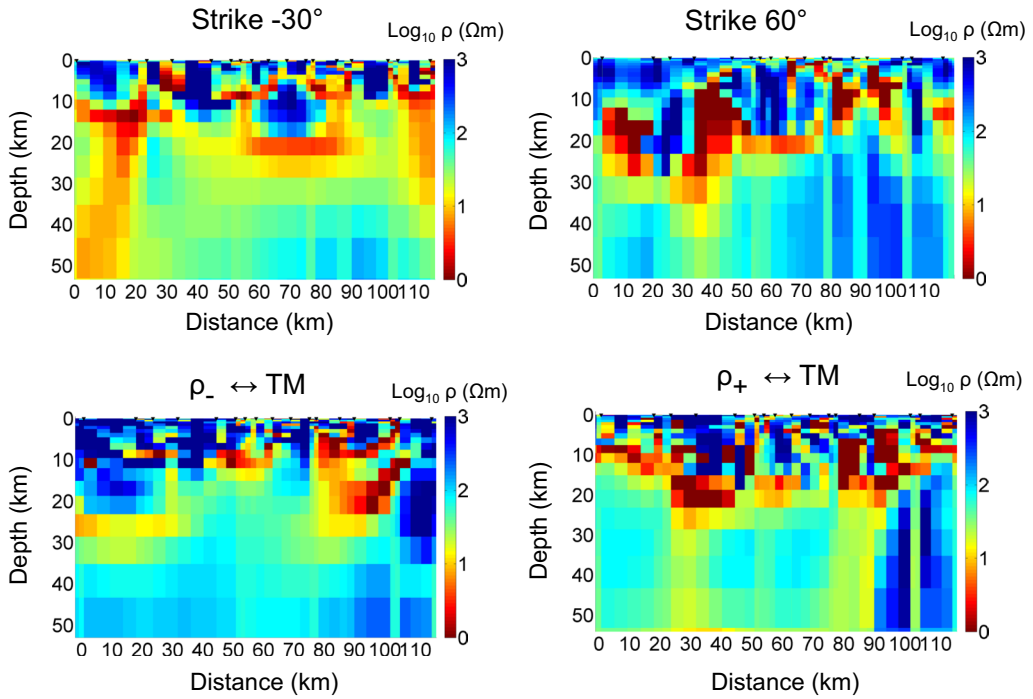

Fig. 8 The roughest models obtained by inverting the amplitude of the TM mode and the phases of both modes. The computed TE apparent resistivities of these models are compared with the corresponding data pseudo-sections in the last four figures

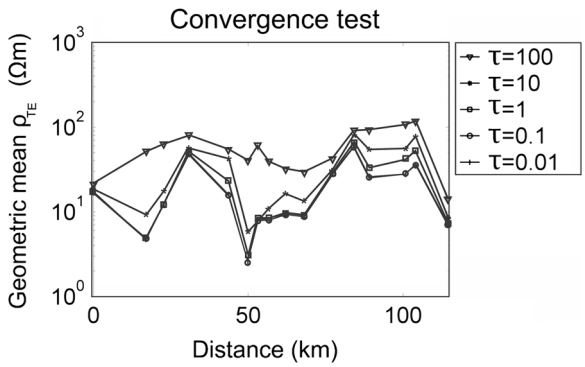

Fig. 9 The roughest models shown in this figure are chosen when the curves of the computed TE apparent resistivity converge as the regularization parameter tau decreases to zero. The graph shows how the geometric mean of the apparent resistivity curves converges for each site

Static shifts

Proceeding with the analysis of the computed TE apparent resistivity pseudo-sections of Figs. 4, 5, 6 and 7, we need to explain why they do look or do not look alike those of the field data, depending on the case. It is difficult to infer what is behind the discrepancies by comparing the images because they present different shapes. To illustrate the differences we chose three sites from the worst and the best resemblances. The worst is ρ_- ↔ TM and the best is ρ_+ ↔ TM. Figure 10 shows the comparison between the computed sounding curves and the field data. It can be observed that the TM data in both cases are well fitted by the corresponding responses of their roughest models and that the TE computed and field curves are parallel to each other. The degree of shift, measured by the ratio of the field curve to the computed response, defines the static-shift factor. The factors for all the sites are shown in Fig. 11 for both ρ_- ↔ TM and ρ_+ ↔ TM. The average factor for the first case is of about two orders of magnitude and always greater than unity. The values of unity at the extremes of the profile were not fixed, that is how they come out in the calculations. On the other hand, the average factor for the second case is of less than an order of magnitude and presents values larger and smaller than unity. These factors for ρ_+ ↔ TM seem more likely than the too large and consistently larger than unity of ρ_- ↔ TM. This is a third and extra point in favor of the NE strike.

It is possible with this dataset to make a classical hypothesis testing exercise. What we did was to take three soundings from each of the pseudo-sections and used them as predictors of how a static-free sounding would look like over the Nelson Batholith. The

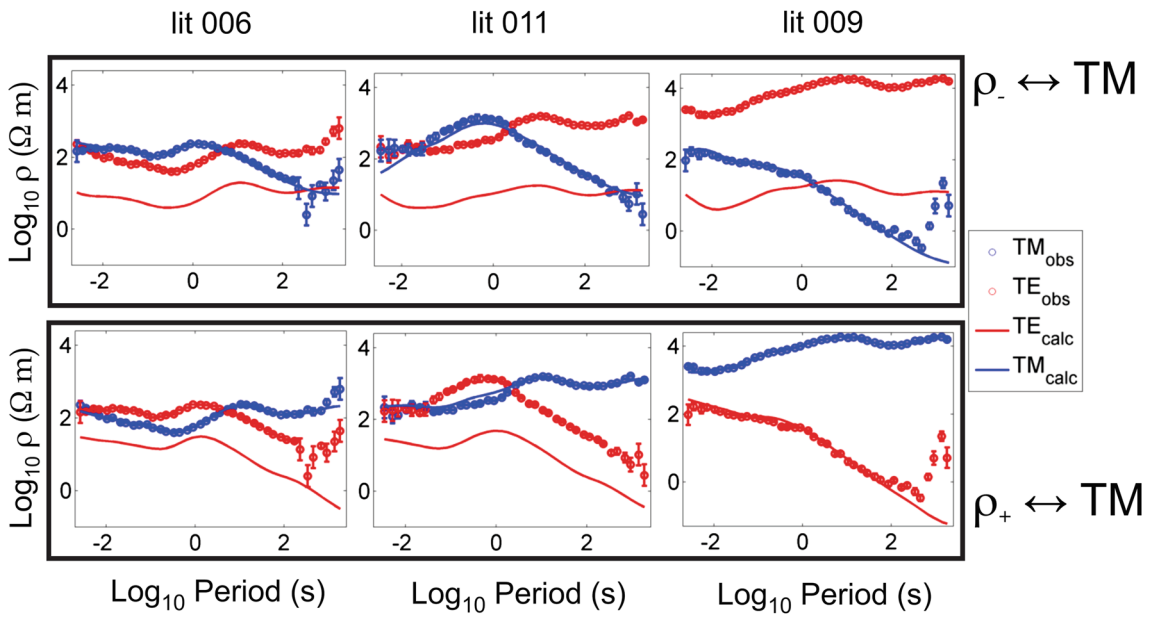

Fig. 10 The effect of leaving the TE apparent resistivity curves out of the inversion process is that the computed TE curves of the roughest models are approximately parallel to the field curves. It can be observed that the shifts for the three sites shown are far larger when assuming that ρ_- is the TM resistivity than when assuming that ρ_+ is the TM resistivity

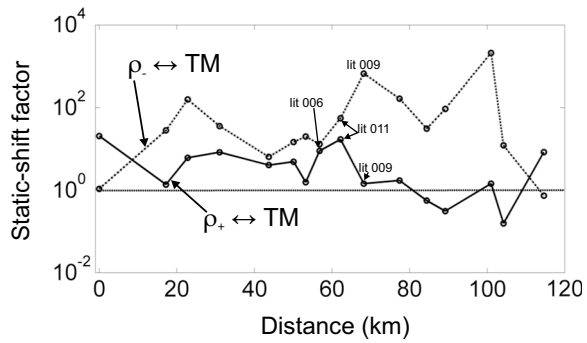

Fig. 11 Static-shift factors for the different sites for the cases of ρ_- ↔ TM and ρ_+ ↔ TM. Notice that factors are about two orders of magnitude larger in the former case than in the latter. The three signaled sites are the same depicted in detail in this figure

predictions are then compared with actual EMAP observations. Figure 12 shows the predictions of the four options contrasted with an EMAP line reported by Jones et al. (1989) whose location is shown in Fig. 3 as lying over the Nelson Batholith. The line is 10 km long and runs with an azimuth N30°W, so that the measured electric fields have the same azimuth as those of the TE mode. It can be observed that the cases of strike N30°W and its associated ρ_- ↔ TM stand as the worst predictions. Next comes N60°E and the best match is its associated ρ_+ ↔ TM. Then there is no doubt, what the hypothesis testing exercise is telling us is that the model behind the ρ_+ ↔ TM option is the best choice. Notice that we are not using the EMAP line to correct the data as it is customary. We are using it as an external agent to help us decide which hypothesis makes the correct prediction. The result supports the hypothesis that the invariant TE and TM impedances associated with ρ_+ ↔ TM should be the best choice. Before proceeding to compare the corresponding models we still have a final point to clarify. The electric fields of the EMAP line have the direction N30°W. That is, the electric dipoles are aligned along the EMAP line. If we assume a strike N60°E the TM mode corresponds also to electric dipoles in the direction N30°W. The same goes for the associated ρ_+ ↔ TM; the electric fields are predominantly NW. Let us now turn to the models or predicted images of the subsurface. They can be contrasted directly with other geophysical methods and with the geology of the area.

Models

We need to convert the static-free pseudo-sections into true sections, in order to compare them with other geophysical models and to make possible geological inferences. To do this we also follow Bostick (1984, 1986) who uses the 1D approximate formulae known as the Nibblet–Bostick transformation (Jones 1983). We use a stable version that estimates depth averages of electrical conductivity by combining data for any two periods

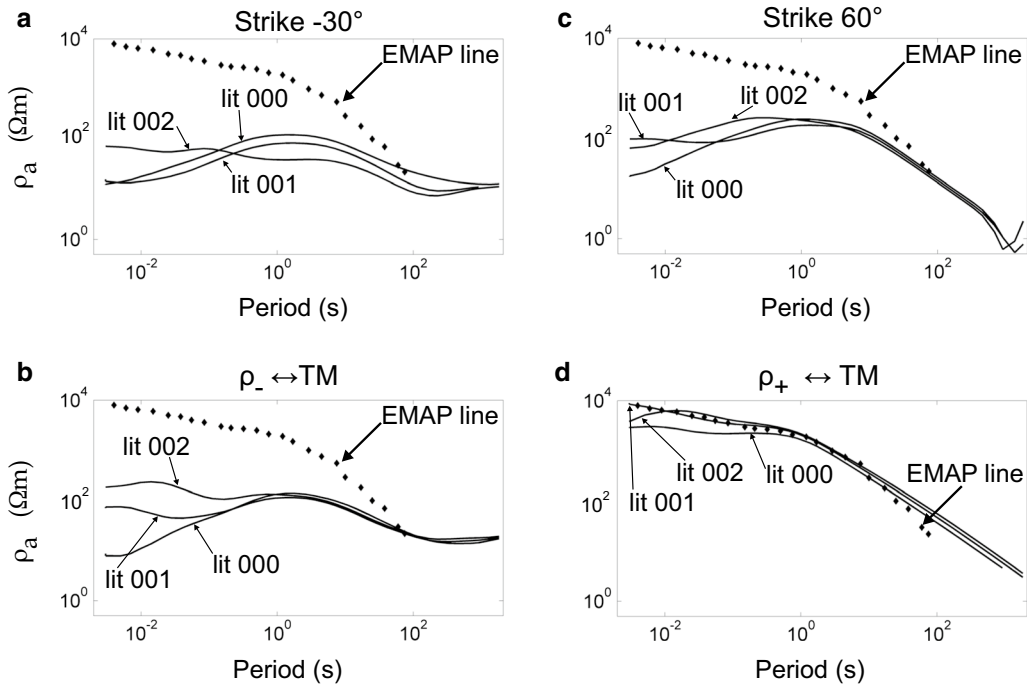

Fig. 12 The predicted static-free TE apparent resistivity curves over the Nelson Batholith contrasted with the EMAP line of Jones et al. (1989). **a** N30°W and **b** its associated invariant ρ_- ↔ TM. **c** N60°E and **d** its associated invariant ρ_+ ↔ TM

(Gómez-Treviño 1996). Expressed in terms of resistivities the formula is

$$\rho_{\mathrm{HA}}(h_1,h_2) = \frac{1}{\frac{1}{h_2-h_1}\int_{h_1}^{h_2}\frac{1}{\rho(z)}dz} = \frac{h_2-h_1}{\frac{h_2}{\rho_{a2}}-\frac{h_1}{\rho_{a1}}}, \quad (10)$$

where

$$h_1 = \frac{\sqrt{2}}{2}\delta_1 = (0.707)503\sqrt{\rho_{a1}T_1}m \quad (11)$$

and

$$h_2 = \frac{\sqrt{2}}{2}\delta_2 = (0.707)503\sqrt{\rho_{a2}T_2}m. \quad (12)$$

The average ρ_{HA} is the harmonic average over depth z of the underground vertical resistivity distribution $\rho(z)$. The average is over a depth window defined by h_2 and h_1.The widths of the depth windows are $h_2 - h_1$, where h_2 and h_1 are fractions of the skin depths δ_1 and δ_2, respectively. The apparent resistivity ρ_{a1} corresponds to the period T_1 and ρ_{a2} to T_2, where it is assumed that $T_1 < T_2$. The values of ρ_{HA} are plotted at the geometric mean $h_m = \sqrt{h_1 h_2}$.

The sections of resistivity versus depth are shown in Fig. 13 in the same order as those of Fig. 12. As expected, the images for N30°W and ρ_- ↔ TM on the left side provide somewhat similar pictures of the subsurface. The same can be said about the images for N60°E and ρ_+ ↔ TM on the right side. However, contrasting left and right sides it is clear that they offer qualitatively different pictures of the subsurface. It is also clear that the choice of N30°W or N60°E is crucial for a correct interpretation. The same applies for the choice between ρ_- ↔ TM or ρ_+ ↔ TM. We spent quite some time working with the pair (N30°W, ρ_- ↔ TM) trying to make sense of the models on the left side of Fig. 13. Then we found out about the existence of the deep transverse basement structural control of mineral systems in the area reported by McMechan (2012), and became fully aware of the results of Eisel and Bahr (1993) for the complementary angle of strike. This motivated the exercise of predicting the EMAP line with the pair (N60°E,ρ_+ ↔ TM). The corresponding resistivity image assuming ρ_+ ↔ TM is shown in Fig. 13d. Basically, this image reveals a large resistive body below the surface expression of the Nelson Batholith. Notice that the image for the fixed angle N60°E is a hesitant disclosure of the resistive body.

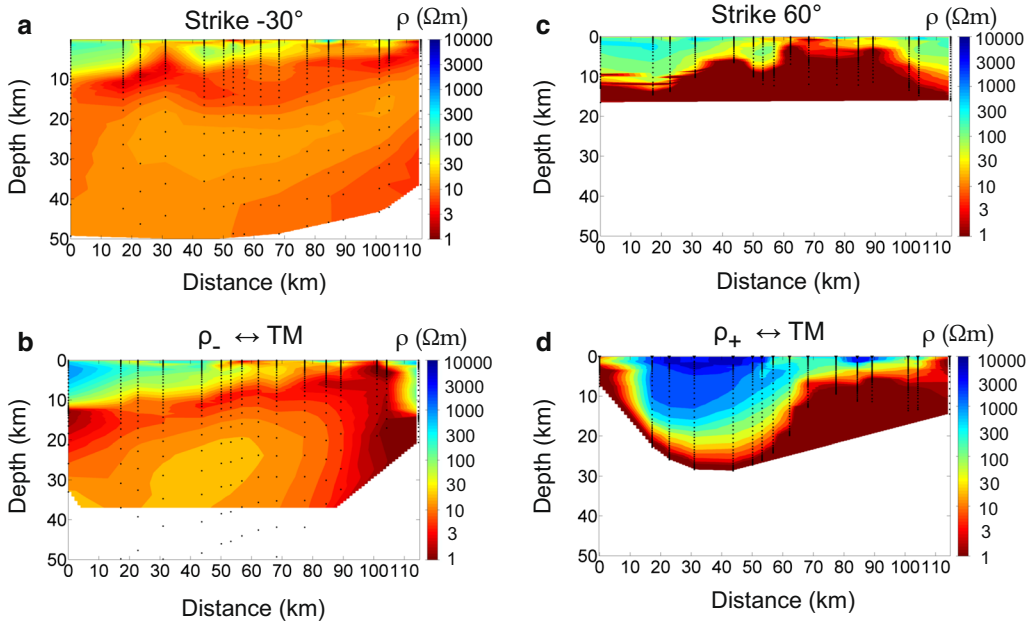

Fig. 13 Images of the subsurface obtained by inverting the four computed TE apparent resistivity pseudo-sections shown in Figs. 5, 6, 7 and 8. These images are in the same order as those in Fig. 10. **a** and **c** are for the two fixed angles and **b** and **d** for the related invariants. The inversion was performed using the 1D formula of Eq. 10 for harmonic averages of resistivity between two depths h_2 and h_1. The dots correspond to the geometric mean $h_m = \sqrt{h_1 h_2}$

In addition to the concordance shown in Fig. 12 in relation with the EMAP line, the image for $\rho_+ \leftrightarrow$ TM clearly delineates the Nelson Batholith which is the prominent geological feature of the profile. This is further confirmed in Fig. 14 by contrasting the resistivity image with the seismic refraction model of Clowes et al. (1995). In the same figure, we include a seismic reflection model from Zelt and White (1995). It can be observed that the resistivity image correlates very well with the two seismic models, and particularly in relation to the location of the Slocan Lake Fault (SLF in the figure).On the other hand, the highly conductive regions below the whole profile and particularly at shallow depths below the Purcell Anticlinorium, are most likely extensions of those detected at also shallow depths by Gupta and Jones (1995) in a more extensive survey of the anticlinorium. They associate the enhanced conductivity to the presence of mineralization (copper, etc.), rather than other geophysical causes. In any case, the depth of penetration is severely damped at the base of the resistivity image because of this enhanced conductivity. It can be observed that the assigned depths for the longest periods all cluster together above the largest penetration. Along the profile they define a kind of envelope or halo that embraces the Nelson Batholith, the Kootenay Arc and the Purcell Anticlinorium. Very little else can be said about this halo beyond its uppermost topography because of the severely damped depths of penetration. This also prevents the detection of an anisotropic layer below 30 km reported by both Jones et al. (1993) and Eisel and Bahr (1993). In any case, even with enough depth of penetration we wouldn't be able to judge about the anisotropic nature of the layer because we are using invariants. Aside from this, our model resembles a lot more that of Eisel and Bahr (1993) who assume a N45°E strike, than that of Jones et al. (1993) who assume a N30°W strike.

The invariant character of the TE and TM impedances relaxes the rigidity of a single strike direction. However, using invariants does not save us from the classical problem of having to choose between two possible strikes. The question is transferred to decide between ρ_+ and ρ_-. In the present case all ρ_- curves have the same shape and also do all ρ_+ curves (see Fig. 10 for a sample). The question is to decide which shape corresponds to which mode. One way is to use the STRIKE algorithm to couple the impedances with a strike direction as we did and then associate by shape the resulting TE and TM modes with the ρ_+ and ρ_- resistivities. In this way, we were able to associate the strike N60°E with $\rho_+ \leftrightarrow$ TM. Our approach still relies on the STRIKE algorithm for this geographical connection with the geology.

We show in Fig. 15 the resistivity image together with estimates of the strike directions using the phase tensor as reported in Muñíz et al. (2017). Of the two

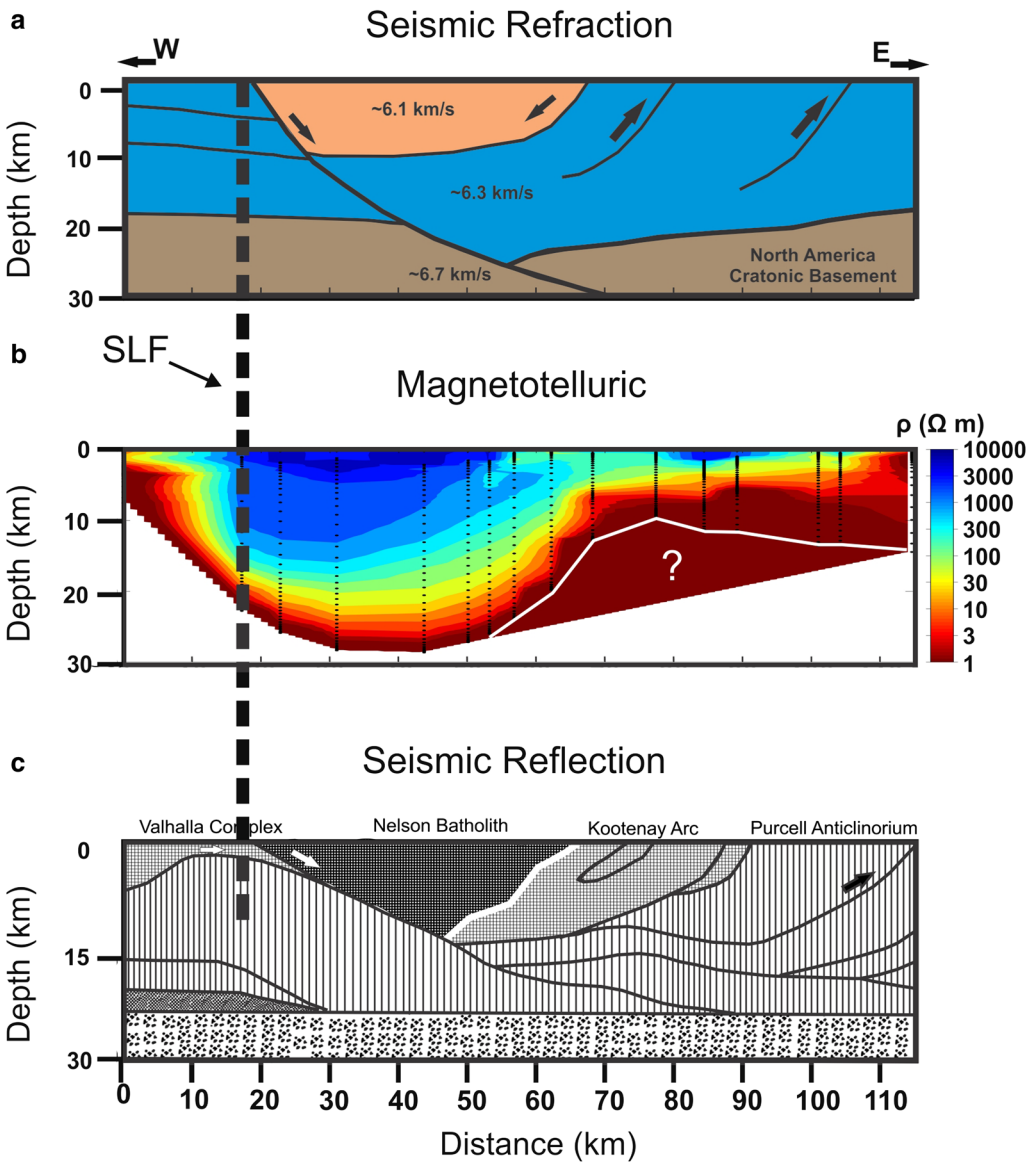

Fig. 14 **a** Seismic refraction model adapted from Clowes et al. (1995). **b** Resistivity image for the case $\rho_+ \leftrightarrow$ TM. **c** Seismic reflection model adapted from Zelt and White (1995). SLF stands for Slocan Lake Fault

complementary angles, we chose only the positive values in view of the mentioned choice of $\rho_+ \leftrightarrow$ TM and its relation with N60°E. Geologically, the strikes correspond to the local transversal structures reported by McMechan (2012). The strikes are plotted using the same vertical scales as for the resistivities. Figure 15 summarizes the results of relaxing the directionality constraints in 2D inversions. On one side we have a resistivity model that complies with a strict requirement as an EMAP line much better than assuming a fixed strike, and on the other we have a detailed strike model of the subsurface. The largest strikes in red around the eastern edge of the Nelson Batholith correspond very well with the newly discovered transversal structures described by McMechan (2012). This may be a chance coincidence but we cannot but mention it because they are the features that stand out in both the strikes image below and the geological map of McMechan (2012).

A final remark about how to view Fig. 15 is worthwhile. The resistivity image comes directly from the TE response of a model with zero strike. However, this model comes from inverting data that may have different strikes. Thus, the resistivity image cannot be viewed as a normal cross section whose properties don't change

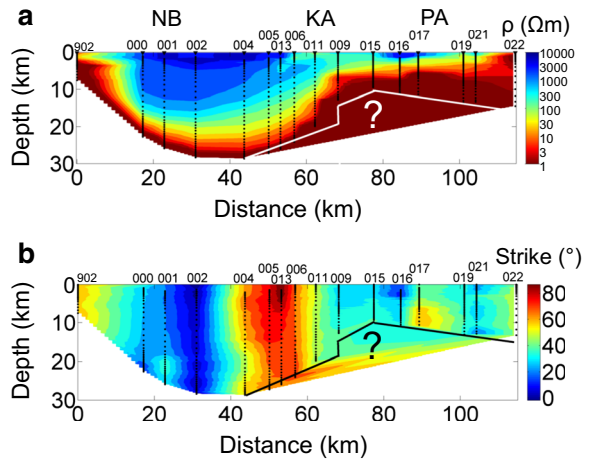

Fig. 15 **a** Resistivity image obtained using invariant data. **b** Corresponding strike directions plotted at the same depths as the resistivity values (modified from Muñíz et al. (2017). NB stands for Nelson Batholith, KA for Kootenay Arc and PA for Purcell Anticlinorium

in the direction perpendicular to the profile, which corresponds to strike zero. It is still a cross section, but now we have to specify the related azimuths. The fit to the data was done assuming a model with azimuth zero, but because the impedances are invariant this model can accommodate perfectly well other azimuths. The model is then incompletely characterized by the resistivity distribution, and requires to be fully differentiated to specify the corresponding distribution of strikes.

Conclusion

The recognition that TE and TM impedances can be treated in theory and in practice as invariants opens a new possibility for treating MT profiles that present inconsistent strikes. The current approach is to fix the strike and modify the impedances accordingly. The new option keeps the invariant impedances untouched in spite of multiple strikes. With the present computing power, there is no reason for not working with both options in routine 2D interpretations. The present work completes earlier developments for removing 1) electro-galvanic distortions using the same quadratic equation as for the present problem, and 2) the static effects using a mimic of the EMAP method. The conclusion that the strike-free impedances are valuable assets for 2D interpretations is presented in three progressive steps using the BC87 dataset. First, they lead to more reasonable static factors than those of fixed strikes. Second, they predict much better an independent EMAP line over the Nelson Batholith. And third, their predicted image of the subsurface correlates very well with seismic refraction and reflection surveys, particularly in relation to the Slocan Lake Fault and the delineation of the Nelson Batholith. We conclude that this is because a model with strike zero can accommodate impedances with other strikes. The resulting resistivity image of the subsurface is no longer a normal cross section. It is still a cross section, but it requires the corresponding strikes to be specified because otherwise the resistivity image is strike ignorant. We hope that he gives a lift to the survival of 2D MT profiles which come so naturally in many matter-of-fact applications.

Abbreviations

MT: magnetotelluric; TE: transverse electric; TM: transverse magnetic; EMAP: electromagnetic array profiling; 2D: two-dimensional; 1D: one-dimensional; SLF: Slocan Lake Fault; NB: Nelson Batholith; KA: Kootenay Arc; PA: Purcell Anticlinorium.

Authors' contributions

YM performed part of the inversions for the first half of the manuscript. MC run the STRIKE algorithm for the fixed angle strikes and the corresponding inversions and her work led to the comparison with the EMAP line. The earlier work of AC with other invariants led to the comparison with the seismic reflection and refraction surveys. EGT developed the theory, drafted the manuscript and coordinated the different steps. All authors read and approved the final manuscript.

Acknowledgements

We would like to thank Alan Jones for providing the BC87 dataset and the new version of the STRIKE algorithm. Thanks also to J.M. Romo, F.J. Esparza and C. Flores for fruitful discussions, and to the anonymous reviewers for helpful comments to shorten and improve the manuscript. Y.M., M.C. and A.C-M acknowledge scholarships from CONACYT. Y. M. and A.C-M. also acknowledge terminal scholarship from CeMIE-Geo through CONACYT Project Number 207032. Thanks also to CeMIE-Geo for the use of the Lamb Cluster for running inversions.

Competing interests

The authors declare that they have no competing interests.

Availability of data and materials

The BC87 dataset is available at the MTNet site (http://www.complete-mt-solutions.com/mtnet/main).

Funding

CICESE, CONACYT and CeMIE-Geo (CONACYT Project Number 207032).

Publisher's Note

Received: 11 April 2018 Accepted: 1 August 2018
Published online: 13 August 2018

References

Berdichevsky MN, Dmitriev VI (1976) Basic principles of interpretation of magnetotelluric curves. In: Adam A (ed) Geoelectric and geothermal studies. Akademiai Kiado, Budapest, pp 165–221

Bostick FX Jr. (1984) Electromagnetic array profiling survey method: U.S. patent 4,591,791

Bostick FX (1986) Electromagnetic array profiling: 56th Annual International Meeting, SEG, Expanded Abstracts, pp 60–61

Cagniard L (1953) Basic theory of the magneto-telluric method of geophysical prospecting. Geophysics 18(3):605–635

Caldwell TG, Bibby HM, Brown C (2004) The magnetotelluric phase tensor. Geophys J Int 158:457–469
Clowes RM, Zelt CA, Amor JR, Ellis RM (1995) Lithospheric structure in the southern Canadian Cordillera from a network of seismic refraction lines. Can J Earth Sci 32(10):1485–1513
Constable SC, Parker RL, Constable CG (1987) Occam's inversion: a practical algorithm for generating smooth models from electromagnetic sounding data. Geophysics 52:289–300
Eisel M, Bahr K (1993) Electrical anisotropy in the lower crust of British Columbia: an interpretation of a magnetotelluric profile after tensor decomposition. J Geomagn Geoelectr 45:1115–1126
Gómez-Treviño E (1996) Approximate depth averages of electrical conductivity from surface magnetotelluric measurements. Geophys J Int 127:762–772
Gómez-Treviño E, Antonio-Carpio R, Romo JM, Esparza F (2013) A recursive set of invariants of the magnetotelluric impedance tensor. Acta Geod Geophys 48(3):265–274
Gómez-Treviño E, Romo JM, Esparza F (2014a) Quadratic solution for the 2-D magnetotelluric impedance tensor distorted by 3-D electro-galvanic effects. Geophys J Int 198:1795–1804
Gómez-Treviño E, Esparza F, Muñiz Y, Calderón A (2014b) The magnetotelluric transverse electric mode as a natural filter for static effects: application to the COPROD2 and COPROD2S2 data sets. Geophysics 79:E91–E99
Groom R, Bailey RC (1989) Decomposition of magnetotelluric impedance tensors in the presence of local three-dimensional galvanic distortions. J Geophys Res 93:1913–1925
Gupta JC, Jones AG (1995) Electrical conductivity structure of the Purcell Anticlinorium in southeast British Columbia and northwest Montana. Can J Earth Sci 32:1564–1583
Jones AG (1983) On the equivalence of the "Niblett" and "Bostick" transformations in the magnetotelluric method. J Geophys 53(1):72–73
Jones AG (1993) The BC87 dataset: tectonic setting, previous EM results, and recorded MT data. J Geomagn Geoelectr 45:1089–1105
Jones AG, Kurtz RD, Oldenburg DW, Boerner DE, Ellis R (1988) Magnetotelluric observations along the lithoprobe southeastern Canadian cordilleran transect. Geophys Res Lett 15:677–680
Jones AG, Boerner DE, Kurtz RD, Oldenburg D, Ellis RG (1989) EMAP data processing in the wavenumber domain. In: SEG annual meeting. Society of Exploration Geophysicists
Jones AG, Groom RW, Kurtz RD (1993) Decomposition and modelling of the BC87 dataset. J Geomagn Geoelectr 45:1127–1150
McMechan ME (2012) Deep transverse basement structural control of mineral systems in the southeastern Canadian Cordillera. Can J Earth Sci 49(5):693–708
McNeice GW, Jones AG (2001) Multisite, multifrequency tensor decomposition of magnetotelluric data. Geophysics 66:158–173
Muñíz Y, Gómez-Treviño E, Esparza FJ, Cuellar M (2017) Stable 2D magnetotelluric strikes and impedances via the phase tensor and the quadratic equation. Geophysics 82(4):E169–E186
Parker RL (2010) Can a 2-D MT frequency response always be interpreted as a 1-D response? Geophys J Int 181:269–274
Pedersen LB, Engels M (2005) Routine 2D inversion of magnetotelluric data using the determinant of the impedance tensor. Geophysics 70:G33–G41
Rikitake T (1950) Electromagnetic induction within the Earth and its relation to the electrical state of the Earth's interior. Bull Earthq Res Inst Tokyo Univ 28:45
Rodi W, Mackie RL (2001) Nonlinear conjugate gradients algorithm for 2-D magnetotelluric inversion. Geophysics 66(1):174–187
Romo JM, Gómez-Treviño E, Esparza F (2005) Series and parallel transformations of the magnetotelluric impedance tensor: theory and application. Phys Earth Planet Int 150:63–83
Swift CM (1967) A magnetotelluric investigation of an electrical conductivity anomaly in the southwestern United States. Doctoral Dissertation, Massachusetts Institute of Technology
Tikhonov AN (1950) On determining electrical characteristics of the deep layers of the Earth's crust. In: Vozoff K (ed) Magnetotelluric method. Geophysics reprint series, vol 5. SocExplGeophys, Tulsa, pp 2–3
Varentsov IM (1998) 2D synthetic data sets COPROD-2S to study MT inversion techniques. In: The 14th workshop on electromagnetic induction in the earth, Sinaia, Romania
Weidelt P, Kaikkonen P (1994) Local 1-D interpretation of magnetotelluric B-polarization impedances. Geophys J Int 117:733–748
Zelt CA, White DJ (1995) Crustal structure and tectonics of the southeastern Canadian Cordillera. J Geophys Res 100:24255–24273